A dual-band gas sensing metastructure based on CPA for H_2 production with SO_2 oxidation reaction

Jia-Hao Zou [a], Jun-Yang Sui [a], Ting-Shuo Yao [a], Hai-Feng Zhang [a,b,*]

[a] *College of Electronic and Optical Engineering & College of Flexible Electronics (Future Technology), Nanjing University of Posts and Telecommunications, Nanjing, 210023, China*
[b] *State Key Laboratory of Millimeter Waves of Southeast University, Nanjing 210096, China*

ARTICLE INFO

ABSTRACT

This paper presents a high-resolution dual-band gas sensing metastructure (GSM) based on coherent perfect absorptivity (CPA), designed for the concentration detection of hydrogen (H_2) and sulfur dioxide (SO_2). By establishing a linear relationship between the frequency shift of the absorptivity peak (AP) and the refractive index variation caused by gas concentration changes, the system simplifies the detection of environmental signals into linear photoelectric signals. Utilizing CPA, the GSM achieves dual-mode sensing for H_2 and SO_2 in different sensitivities through phase control. For H_2 concentration sensing, the two modes exhibit sensitivities of 8.84 THz/RIU and 2.3 THz/RIU, respectively. For SO_2, the sensitivities are 46.8 THz/RIU and 17.76 THz/RIU. Moreover, for the sensing of both gases, excellent sensing performance can be achieved (high-quality factor is larger than 8.0×10^4 and detection limit is less than 2×10^{-7} RIU). This combining CPA dual-band GSM, offers enhanced accuracy compared with single-band sensors, and provides a promising advancement for future measurement technologies.

1. Introduction

Hydrogen gas (H_2), made of the simplest and most abundant element in the universe, holds immense promise as a clean and efficient energy source [1,2]. Water electrolysis is the currently important electrochemical process used to produce H_2 [3], but it is limited by the oxygen evolution reaction (OER) [4,5], which needs high energy. Because sulfur dioxide (SO_2) oxidation reaction (SO_2OR) with coupled water electrolysis, which can consume an abundant pollutant and generate Sulfuric acid (H_2SO_4), requires less energy, the process for H_2 production is deemed to be a new way to handle the problems of the OER [5]. The supplement material section 1 roughly depicts this production process. However, the raw materials and products (SO_2 and H_2) of the industrial process present safety and environmental challenges [6–9]. Due to its highly flammable nature (its explosion limit is 4.0 % ~ 75.6 %), the leakage of H_2 is hazardous [10]. SO_2 is a noxious gas that is a byproduct of various industrial processes and combustion activities, and it is also found in volcanic emissions and some environmental contexts [8,9]. Because both SO_2 and H_2 have detrimental effects on human health and

the environment, accurate monitoring and control of SO_2 and H_2 emissions in H_2 production with SO_2OR are critical.

Currently, there are several technologies that enable gas sensing, like electrochemical gas sensors [11–13], semiconductor gas sensors [14–17], thermal conductivity gas sensors [18], chemiluminescent gas sensors [19], and optical gas sensors [20,21]. Due to the high responsiveness of electromagnetic waves (EWs), optical gas sensors have been paid more attention [22,23]. Optical gas sensors can be realized by nondispersive infrared measurement [24], photoacoustic spectrum analysis [25], optical fiber [26], and metastructure [27–31]. Because gas sensing metastructure (GSM) has wide applications in industrial, medical, and environmental [27], it has been studied extensively in recent years. Danasegaran *et al.* [32] designed a susceptible GSM based on a micro-ring resonator for detecting various toxic gases. Kumar *et al.* [33] developed a GSM with a designed defect cavity based on materials of dielectric layers with zero value of extinction coefficient. Zhang *et al.* [34] proposed a dual-band GSM based on Tamm plasmon polaritons and Fabry-Perot. These pieces of work are crucial for the development of gas sensing and offer a novel perspective on GSM research. Nevertheless,

---

there is a lack of optical gas sensors that integrate H_2 and SO_2 sensing capabilities, and these works are unable to achieve both a relatively high-quality factor (Q) (about 8×10^4) and a relatively low detection limit (DL) (2×10^{-7} RIU).

Furthermore, it is difficult to realize dual-band gas sensing without changing the physical properties of GSM. Realizing dual-band sensing may find a new way to develop the field of analytical chemistry [35]. Combining coherent perfect absorptivity (CPA) [36–38] with GSM may provide a new inspiration for the development of dual-band sensing technology. The phase difference of the coherent EWs is also an important factor in generating the absorptivity peak (AP), in addition to the physical properties of GSM. By changing the phase difference, the EWs response of GSM will be reshaped, that is, the sharp AP will appear at different frequency points in the case of different phase differences [39–42].

Herein, a layered dual-band GSM with high resolution based on CPA integrating H_2 and SO_2 sensing functions is proposed in this paper. Because near-infrared (from 128 THz to 428 THz), which plays an important role in the field of sensing [43,44], has strong penetration ability and is easier to form high-resolution sensing, the GSM proposed in this paper works in near-infrared. In addition, it should be noted that this work focuses on the simulation-based point of view while concentrating on theoretical innovation due to the difficulty of funding and experimental conditions. The conclusions are all supported by previously published research and are calculated using industry-accepted tools [45–48]. As a result, the conclusions in this work are reasonable and rigorous. In this study, the frequency point corresponding to the AP shifts as the refractive index (RI) of the analysis layers changes. The frequency point of the AP exhibits a strong linear relationship with the detection RI, with an R-squared value of 1. It is possible to transform the undetectable environment signal into a linear observable photoelectric signal. Moreover, this work proposes a new way of applying CPA to optical measurement techniques. With the help of CPA, the GSM can realize dual-band detection by phase control. The GSM performance parameters for gas sensing are not the same (For H_2 concentration sensing, the two modes exhibit sensitivities of 8.84 THz/RIU and 2.3 THz/RIU, respectively. For SO_2, the sensitivities are 46.8 THz/RIU and 17.76 THz/RIU) due to two different sensing band. Compared with traditional GSM, this work can not only achieve excellent gas sensing performance (higher Q and lower DL) but also increase the reliability of sensing through realizing dual-band sensing. Because of its benefits in detecting both H_2 and SO_2, the proposed GSM could be applied in the H_2 production with SO_2 oxidation reaction [5], and it may be significant for future measurement technologies.

2. Structure design and theoretical calculation

2.1. The configuration of GSM

The GSM is a layered structure, which can be seen in Fig. 1. To more clearly display the construction of the proposed GSM, different dielectrics are labeled with different colors in Fig. 1 **(a)**. The GSM consists of ordinary dielectrics barium strontium titanate (BST) [49], Zinc germanium phosphide (ZnGeP$_2$) [50], and gallium sulfide (GaS) [51], which respectively are regarded as dielectric A, B, and C. Among them, BST is doped with 10 wt% magnesium oxide (MgO), and its RI n_A can reach 16.49 [33]. The values of RIs belonging to ZnGeP$_2$ and GaS, which are regarded as n_B and n_C, in this paper are defined as 3.14 and 2.72 [50,51]. These dielectrics form periodic structures, and the number of stacking cycles N_0 is 4. In the middle of the structure, the core gas sensing part is made up of the analysis layer and combination layers (CL). As can be seen in Fig. 1 **(b)**, hydrogen-sensitive film [52] (does not react with SO_2) and gas layer compose the analysis layer. As the H_2 concentration, C_H in the air increases from 0 to 4 %, the RI of hydrogen-sensitive film n_{eff} falls from 1.995 to 1.992 [50]. The linear relationship between the n_{eff} and C_H is created by the experimental findings from
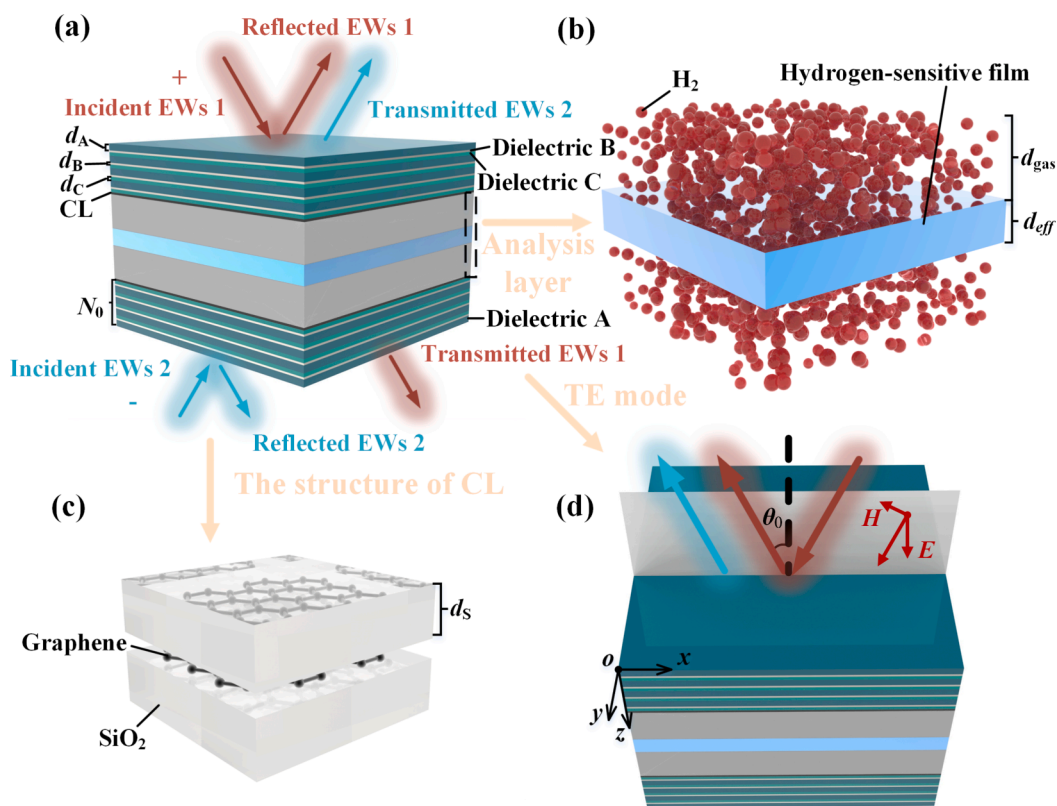
Fig. 1. Schematic representation of the GSM, which consists of different dielectric layers. (a) Theoretical structure diagram of GSM, (b) The specific structure of the analysis layer, (c) The specific structure of CL, and (d) Electromagnetic waves interact with the GSM in TE mode.

Ref. [52]:

$$n_{eff} = 1.995 - 0.067C_H.$$ (1)

In this paper, the RI of air-mixed gas is defined as n_{gas}. The effect of C_H on n_{gas} is negligible, but the concentration of SO_2 C_{SO2} has a great effect on n_{gas}. The relationship between the n_{gas} and C_{SO2} can be expressed as a linear equation [53]:

$$n_{gas} = n_{air}(1 - C_{SO2}) + n_{SO2}C_{SO2},$$ (2)

where n_{SO2} is considered as 1.341, and n_{air} is regarded as the RI of normal air, i.e. 1. According to Eq.(2), when C_{SO2} increases to 0.5 %, the value of n_{gas} will change to 1.0017.

Fig. 1 **(c)** displays that each CL consists of a graphene layer and silicon dioxide (SiO_2). The RI of SiO_2 n_S is defined as 1.5 [54]. The graphene layer, being a two-dimensional material, has a thickness of just 0.34 nm [55]. Additionally, since no external voltage is applied, the chemical potential (μ_C) of graphene in this study is 0.001 eV [56]. d_i (where i represents A, B, C, S, *eff*, and gas) denotes the thickness of the dielectric layers. Detailed parameters of the GSM are listed in Table 1. The positive z direction of the structure is defined as the direction of the wave vector k at vertical incidence. Since the proposed GSM is a one-dimensional layered structure, the positive x direction and the positive y direction are relative, and the specific definition is shown in Fig. 1 **(d)**. When the EWs are normally incident, both the dielectric materials and graphene respond similarly to the transverse electric (TE) and transverse magnetic (TM) modes [57]. However, under oblique incidence, the graphene layer predominantly responds to the TE mode, with the TM mode having a less pronounced effect [57]. Therefore, this paper focuses solely on the performance of EWs under the TE mode. In this mode, as can be seen in Fig. 1 **(d)**, the wave vector k and the magnetic field H of EWs lie on the *xoz*-plane, and the electric field E is parallel to and along the y-axis. The angle between the EWs and the z-axis negative half shaft is represented as θ_0 (incident angle).

2.2. The manufacturing method of the GSM

Although, the given layered structure of GSM is a theoretical design. But, it can be manufactured by physical vapor deposition (PVD) [58,59], femtosecond laser drilling [60,61], or wet anisotropic etching technique [62]. Among them, PVD has more advantages in the optical fabrication [63]. The thin film deposition methods have been demonstrated to be able to control the thickness and optical parameters at high accuracy [64,65]. The process consists of four steps [58,65]: (i) Atoms from the surface of the material to be deposited are evaporated by a high-energy source, such as an electron beam or ions; (ii) The vapor is transported to the substrate to be coated; (iii) During the transport stage, the metal atoms react with the appropriate reactive gas (such as oxygen, nitrogen, or methane); (iv) The coating is then applied to the substrate surface. The supplementary material describes the preparation process in more detail, as well as the process of transferring graphene to the substrate.

2.3. The formula of the graphene layer

The conductivity σ of the graphene layer is determined by σ_{intra} and σ_{inter} [45,46]:

$$\sigma = \sigma_{intra} + \sigma_{inter},$$ (3)

Table 1
The Detailed Parameters of The GSM.

Parameters	d_A	d_B	d_C	d_{eff}	d_{gas}	d_s
Value (μm)	0.4	0.1	0.2	1	2	0.1
Parameters	n_A	n_B	n_C	n_S	n_{gas}	N_0
Value	16.49	3.14	2.72	1.5	1	4

$$\sigma_{intra} = \frac{ie^2 k_B T_0}{\pi\hbar^2(\omega + i/\tau)}\left(\frac{\mu_C}{k_B T} + 2\ln(e^{-\frac{\mu_C}{k_B T}} + 1)\right),$$ (4)

$$\sigma_{inter} = \frac{ie^2}{4\pi\hbar}\ln\left(\frac{2|\mu_C| - \hbar(\omega + i/\tau)}{2|\mu_C| + \hbar(\omega + i/\tau)}\right),$$ (5)

where ω, k_B, and e severally correspond to the angular frequency, Boltzmann constant, and electron charge. The chemical potential of graphene and reduced Planck constant are regarded as μ_C and $\hbar$. i is an imaginary unit and is equal to $(-1)^{1/2}$. Relaxation time τ is defined as 1 $\times$ 10^{-13} s [45]. Furthermore, because 270 K is the temperature T_0 of air to which the GSM is exposed. The effective dielectric constant ε_g can be counted by [45]:

$$\varepsilon_g = 1 + \frac{i\sigma}{\omega\varepsilon_0 d_g},$$ (6)

where $d_g = 0.34$ nm, which is regarded as the thickness of the graphene layer [45,55], and ε_0 is the vacuum permittivity constant. Furthermore, the RI of the graphene layer can be indicated as $n_g = (\varepsilon_g)^{1/2}$.

2.4. The formula of CPA

The matrix of the EWs propagation for TE mode can be expressed as [47]:

$$\mathbf{M}_j = \begin{pmatrix} \cos(k_{jz}d_j) & -\frac{i}{\eta_j}\sin(k_{jz}d_j) \\ -i\eta_j\sin(k_{jz}d_j) & \cos(k_{jz}d_j) \end{pmatrix},$$ (7)

where $k_{jz} = \omega/cn_j\cos\theta_j$ is the component of k in the z-axis, and c is the speed of EWs in a vacuum. The θ_j satisfies $\sin(\theta_j)/\sin(\theta_0) = n_0/n_j$. The $\eta_i = (\varepsilon_0/\mu_0)^{1/2}n_i\cos\theta_i$ is optical admittance, and μ_0 is the permeability in a vacuum. d_j and n_j express the thickness and RI belonging to every dielectric layer (j can be indicated by A, B, C, S, *eff*, gas, and *g*). The matrix of GSM $\mathbf{M}$ can be written as [47]:

$$\mathbf{M} = \prod \mathbf{M}_j,$$ (8)

which can also be shown like this:

$$\mathbf{M} = \begin{pmatrix} \mathbf{M}_{11} & \mathbf{M}_{12} \\ \mathbf{M}_{21} & \mathbf{M}_{22} \end{pmatrix}.$$ (9)

The following formula can calculate the transmissivity t and the reflectivity r [47].

$$r = \frac{\eta_0(\mathbf{M}_{11} + \eta_0\mathbf{M}_{12}) - (\mathbf{M}_{21} + \eta_0\mathbf{M}_{22})}{\eta_0(\mathbf{M}_{11} + \eta_0\mathbf{M}_{12}) + (\mathbf{M}_{21} + \eta_0\mathbf{M}_{22})},$$ (10)

$$t = \frac{2\eta_0}{\eta_0(\mathbf{M}_{11} + \eta_0\mathbf{M}_{12}) + (\mathbf{M}_{21} + \eta_0\mathbf{M}_{22})},$$ (11)

where $\eta_0 = \eta_{N+1} = (\varepsilon_0/\mu_0)^{1/2}n_0/\cos\theta$ because of both the positive and negative scales exposed to the air. The intrinsic absorptivity (A) of the GSM can be given as [47]:

$$A = 1 - |r|^2 - |t|^2.$$ (12)

The t and r of positive and negative scales are symbolized as "+" and "-". Because the structure of the proposed GSM in this paper is symmetrical, $r = r_+ = r_-$ and $t = t_+ = t_-$ are satisfied. The transmitted EWs from the incident EWs on the other side and the reflected EWs from the incident EWs on this side combine to form the observed EWs O_+ and O_- on each side. This relationship can be explained by using the scattering matrix $\mathbf{S}$ [48]:

$$\begin{pmatrix} O_+ \\ O_- \end{pmatrix} = \mathbf{S} \begin{pmatrix} I_+ \\ I_- \end{pmatrix} = \begin{pmatrix} t & r \\ r & t \end{pmatrix} \begin{pmatrix} I_+ \\ I_- \end{pmatrix}, \tag{13}$$

where I_+ and I_- denote the EWs intensities of the two separate scales. Moreover, Eq.(13) can also be written as follows [48]:

$$O_+ = r|I_+|e^{i\varphi_+} + t|I_-|e^{i\varphi_-}, \tag{14}$$

$$O_- = t|I_+|e^{i\varphi_+} + r|I_-|e^{i\varphi_-}, \tag{15}$$

where φ_+ and φ_- are separately regarded as the phases of the two beams. So, the coherent absorptivity (A_c) can be calculated by [48]:

$$A_c = 1 - \frac{|O_+|^2 + |O_-|^2}{|I_+|^2 + |I_-|^2}. \tag{16}$$

According to Eqs.(13)-(16), the equation about A_c can be resolved to:

$$A_c = 1 - (|t| - |r|)^2 - 2|t||r| \left(1 + \frac{2|I_+||I_-|\cos\Delta\varphi_1\cos\Delta\varphi_2}{|I_+|^2 + |I_-|^2} \right), \tag{17}$$

where $\Delta\varphi_1 = \text{Arg}(t)-\text{Arg}(r)$, and $\Delta\varphi_2 = \varphi_+-\varphi_-$. Among them, "Arg()" is used to represent the argument of a complex number.
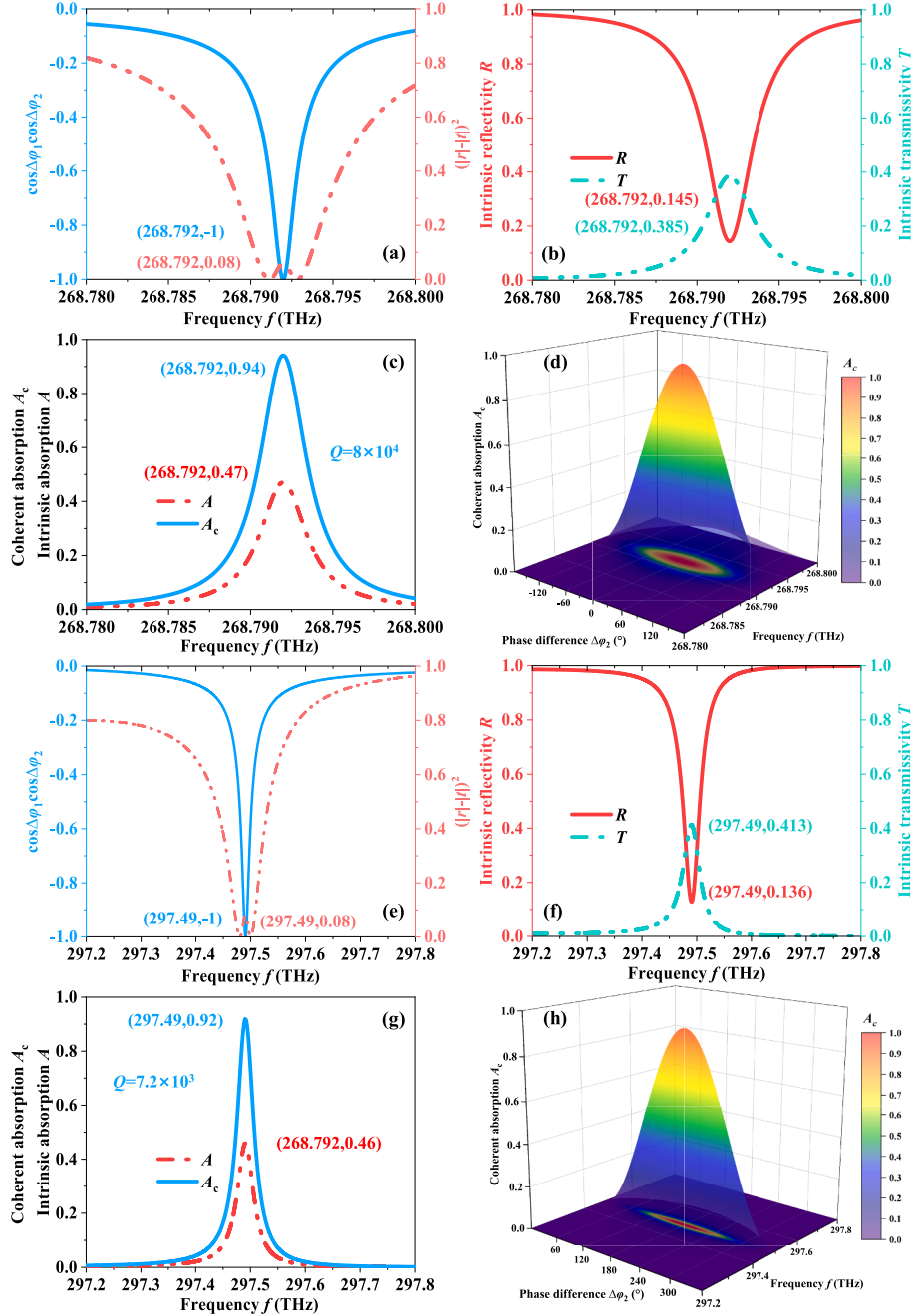
Fig. 2. Simulation data diagrams when the value of $C_H = 4\%$ and $C_{SO2} = 0\%$ at about 268.792 THz or the value of $C_H = 4\%$ and $C_{SO2} = 0\%$ at about 297.49 THz. (a)The curves of $\cos\Delta\varphi_1\cos\Delta\varphi_2$ and $(|r|-|t|)^2$ in the case of $\Delta\varphi_2 = 0°$, (b) The R and T curves as a function of the EWs frequency, and (c) The curves of A_c and A as a function of the EWs frequency. (d) The effects of the $\Delta\varphi_2$ and EWs frequency on the A_c. (e)The curves of $\cos\Delta\varphi_1\cos\Delta\varphi_2$ and $(|r|-|t|)^2$ in the case of $\Delta\varphi_2 = 180°$, (f) The R and T curves as a function of the EWs frequency, and (g) The curves of A_c and A as a function of the EWs frequency. (h) The effects of the $\Delta\varphi_2$ and EWs frequency on the A_c.

3. Analysis and Discussion

3.1. The generation of sharp APs

Q is one important metric for evaluating sensing systems based on APs [66]:

$$Q = \frac{f_T}{FWHM},\qquad(18)$$

where f_T implies the frequency point of AP, and *FWHM* symbolizes the full-width half-maximum of the corresponding peak [66]. The higher Q illustrates a better quality of the GSM [66]. Because the GSM realizes the function of gas sensing based on the value of A_c. The closer the value is to 1, the better the sensing performance. Performance options were discussed in the supplement material section 3.

When the phase difference $\Delta\varphi_2$ is defined to $0°$, detailed simulation data diagrams are gained by the transfer matrix at about the frequency point of 268.792 THz. When the phase difference $\Delta\varphi_2$ is defined to $180°$, detailed simulation data diagrams are gained by the transfer matrix at about the frequency point of 297.49 THz. Fig. 2 **(a)** displays the curves of $\cos\Delta\varphi_1\cos\Delta\varphi_2$ and $(|r|-|t|)^2$. It can be seen from the change of the blue solid line that the value of $\cos\Delta\varphi_1\cos\Delta\varphi_2$ reaches -1 at 268.792 THz, which indicates $\Delta\varphi_1$ and $\Delta\varphi_2$ meet the phase condition for CPA. The change of the red dotted line shows that the value of $(|r|-|t|)^2$ is close to 0 at 268.792 THz. Because the phase and EWs intensity conditions are satisfied at the same frequency point, the CPA is achieved at 268.792 THz in the case of $\Delta\varphi_2 = 0°$. Fig. 2 **(b) and (c)** respectively show the curves of intrinsic reflectance R, intrinsic transmittance (T), A, and A_c. The diagram of A_c can be obtained by resolving Eq.(10). A sharp AP is formed at about 268.792 THz, and the values of A_c and Q are up to 0.94 and 8×10^4. It can be seen from the three-dimensional plot Fig. 2 **(d)** that the value of A_c can be arbitrarily modulated by controlling $\Delta\varphi_2$.

At about 268.792 THz, in the case of $\Delta\varphi_2 = 0°$, the maximum value of A_c reaches 0.94. As $\Delta\varphi_2$ improves, A_c continually declines. The minimum value of A_c is close to 0. Fig. 2 **(e)** shows that phase and EWs intensity conditions are satisfied at the same frequency point (297.49 THz). The two points are (297.49,-1) and (297.49,0.08). So, CPA can be realized at a specific frequency point. As can be seen in Fig. 2 **(f) and (g)**, the values of R, T, and A are 0.136, 0.413, and 0.46, respectively. A sharp AP appears at about the frequency point of 297.49 THz, and the values of A_c and Q are up to 0.92 and 7.2×10^3. It can be seen in Fig. 2 **(h)** that in the case of $\Delta\varphi_2 = 180°$, the maximum value of A_c reaches

0.92. As $\Delta\varphi_2$ decreases, A_c continually declines. The minimum value of A_c is close to 0 when the value of $\Delta\varphi_2$ is $0°$. Moreover, compared with the APs in the case of $\Delta\varphi_2 = 0°$, although the two characteristic frequency points are adjacent, the value of Q is ten times smaller in the case of $\Delta\varphi_2 = 180°$, which is necessary to build dual-band GSM. This demonstrates the advantage of phase controlling based on CPA.

3.2. The analysis for the reason of sharp AP

To better understand how EWs propagate in the GSM and provide an explanation for why sharp AP forms, Fig. 3, which is in the case of $C_H = 4\%$ and $C_{SO2} = 0\%$, at the frequency point of 268.792 THz, is constructed. A microcavity is formed in the structure of the GSM by the intermediate layers (the analysis layer in Fig. 1), which is introduced as the defect layer [67,68]. So, the energy is localized in the middle of the structure, like standing waves [69], shown in Fig. 3 **(a)**. Because of energy localization [70], as can be seen in the supplement material section 4, the GSM at the frequency point of about 268.78 THz forms a sharp peak of T when the graphene layer does not exist, and the T can reach 1, i.e., completely transmitted. To achieve CPA, a graphene layer is added to the structure to regulate the intensity and phase of transmitted and reflected EWs, which meet the regulation of CPA, like Fig. 2. Moreover, as the electric field intensity distribution can be seen, the electric field intensity is higher when two coherent EWs are present and meet the conditions of CPA, as shown in Fig. 3 **(b)**, than when there are only one incident EWs, as shown in Fig. 3 **(a)**. Additionally, as can be seen in Fig. 3 **(c)**, the phase condition between the two incident EWs breaks CPA. Although it is also double-ended, the electric field intensity is far less than the electric field intensity in Fig. 3 **(b)**. A strong absorptivity characteristic is produced at the defect point when two coherent EWs meet the conditions of CPA, which leads to a greater local field augmentation effect. On the contrary, it will break the energy localization.

3.3. The concentration detection of H_2 and SO_2

The technique of frequency modulation, the most often used method, can convert the unobservable physical quantity into an observable optical signal such as the S-parameter by seeking the relationship between the frequency point between the parameter to be measured [56]. Because there is a linear relationship between the n_{eff} and the C_H as Eq. (1), therefore the GSM can realize the detection for C_H by establishing
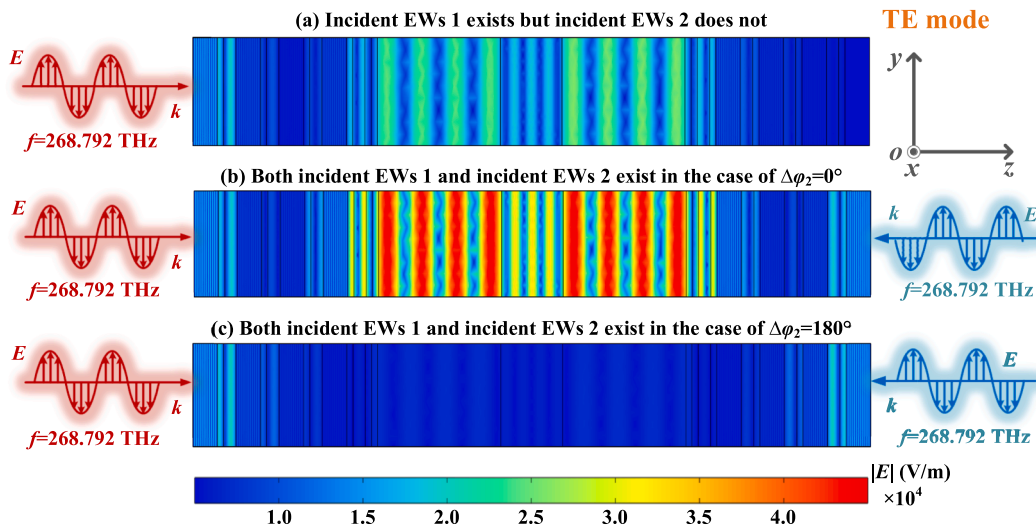
Fig. 3. The electric field intensity distribution maps in the case of $C_H = 4\%$ and $C_{SO2} = 0\%$ when the frequency point of EWs is 268.792 THz. (a) Incident EWs 1 exists but incident EWs 2 does not, (b) Both incident EWs 1 and incident EWs 2 exist, and $\Delta\varphi_2$ is $0°$ (meet the conditions of CPA), and (c) Both incident EWs 1 and incident EWs 2 exist, and $\Delta\varphi_2$ is $180°$ (break the conditions of CPA).

the equation between the AP and n_{eff} in this paper [52,53]. To assess the performance of the sensing, the crucial metrics, which include Q, DL, sensitivity (S), and the figure of merit (FOM), are taken into account in this work. The related formulas can be written as follows [66]:

$$S = \frac{\Delta f}{\Delta x}, \tag{19}$$

$$FOM = \frac{S}{FWHM}, \tag{20}$$

$$DL = \frac{f_T}{20SQ}, \tag{21}$$

where the f_T implies the frequency point of the peak value belongs to AP. The Δf and Δx respectively describe the difference in the frequency and sensing quantity. If the GSM has higher S, Q, and FOM, and lower DL, its quality is better [66].

Through the varying n_{eff} and n_0, the frequency shift spectral line of sensing is obtained. High-Frequency Simulator Structure (HFSS) is based on the finite element method, and the formula in this paper is based on the analytical solution method. Fig. 4 shows the specific setting for simulation with HFSS. Right above the x-o-y plane is the Floquet Port. Because the proposed GSM is a one-dimensional structure, Slave Boundary and Master Boundary are relative. For details, refer to Fig. 4. Because of the truncation error in the calculation of data values, there are differences between the simulation results produced by various methods, for example, the characteristic frequencies do not coincide exactly. After calculation, the error of the two simulation methods is 0.01 THz at most. The error of 0.01 THz is only 0.01 % when compared to the frequency band in which this GSM operates. So such a small error is acceptable. It is possible to confirm the accuracy and dependability of the work outcomes using the outputs of two distinct algorithms.

The vertically incident coherent EWs are emitted respectively from the top and bottom of the unit, which are the Floquet ports. The boundary conditions are set to primary-secondary mode in HFSS. When the GSM is working for C_H sensing, Fig. 5 (a)-(d) displays the change of frequency point with n_{eff} varying in the range of 1.990 ~ 1.995. The results of theoretical values and HFSS are near-identical. As can be seen in Fig. 5 (a), when the $\Delta\varphi_2$ is fixed to 0°, there is a large frequency point shift of the AP in the sensing range. In the case of $n_{eff} = 1.990$, the AP forms at about 268.809 THz. When the value of n_{eff} improves to 1.995, the frequency point correspondingly moves to about 268.765 THz. With the help of contour lines $A_c = 0.9$, it is obvious that the peak values of the APs in the sensing range are all larger than 0.9 which can guarantee the accuracy of the GSM.

Identically, in the case of $\Delta\varphi_2 = 180°$, there is also a frequency point shift of the AP in the sensing range. But the frequency point shift is smaller than the shift in the case of $\Delta\varphi_2 = 0°$. As can be seen in Fig. 5 (b), the AP belonging to $n_{eff} = 1.990$ is formed at about 297.496 THz. When the value of n_{eff} changes to 1.995, which means $C_H = 0$ %, the frequency point of AP also moves to 297.485 THz. Additionally, there is a strong

linear link between the frequency point of AP and the value of n_{eff}. So, the linear fitting relationship of two different $\Delta\varphi_2$ is constructed in Fig. 6 (a).

To clearly analyze the linear fitting relationship, the work also calculates the coefficient of determination (R-square) in the regression model to estimate the degree of fit [66]. The closer it is to 1, the better the fit [66]. When the GSM is working for C_H sensing, the linear fitting relationship of the theoretical results in the case of $\Delta\varphi_2 = 0°$ is $f_1 = -8.84n_{eff} + 286.4$ ($S_1 = 8.84$ THz/RIU), and the linear fitting relationship of the theoretical results in the case of $\Delta\varphi_2 = 180°$ is $f_2 = -2.3n_{eff} + 302.1$ ($S_2 = 2.3$ THz/RIU). The excellent linearity between n_{eff} and f in the sensing range is shown by the R-square up to 1. The supplement material section 5 displays that the values of Q, FOM, and DL respectively are about 8×10^4, 2.6×10^3 RIU^{-1}, and 1.4×10^{-7} RIU when the frequency point changes in the case of $\Delta\varphi_2 = 0°$. When the frequency point changes in the case of $\Delta\varphi_2 = 180°$ the values of Q, FOM, and DL are about 7.55×10^3, 58.5 RIU^{-1}, and 5.75×10^{-6} RIU, respectively.

When the GSM is working for C_{SO2} sensing, Fig. 5 (e)-(h) displays the change of frequency point with n_0 varying in the range of 1.000 ~ 1.004. Compared with the results obtained by simulation software, the results of MATLAB and HFSS are near-identical. As shown in Fig. 5 (e), when the value of n_0 from 1.000 moves to 1.002, the frequency point of AP also changes with it in the case of $\Delta\varphi_2 = 0°$, from 268.765 THz shift to 268.671 THz. In the case of $\Delta\varphi_2 = 180°$, the frequency point of AP also can move (from about 297.485 THz to 297.45 THz) as the value of n_0 changing from 1.000 to 1.002, shown in Fig. 5 (f). It is obvious that the frequency point shift in the case of $\Delta\varphi_2 = 0°$ is larger than in the case of $\Delta\varphi_2 = 180°$. So, different S (S_1 and S_2) can be obtained by controlling the phase. Furthermore, there is also a strong linear relationship between the frequency point of AP and the value of n_0. Fig. 6 (b) displays the linear fitting relationship of the strong linear relationship in Fig. 5 (e) and (f). When the GSM is working for C_{SO2} sensing, the linear fitting relationship of the theoretical results in the case of $\Delta\varphi_2 = 0°$ is $f_1 = -46.8n_0 + 315.6$ ($S_1 = 46.8$ THz/RIU), the linear fitting relationship of the theoretical results in the case of $\Delta\varphi_2 = 180°$ is $f_2 = -17.76n_0 + 302.1$ ($S_2 = 17.76$ THz/RIU), and the R-square can reach 1. As the frequency point varies in the situation of $\Delta\varphi_2 = 0°$, the supplement material section 5 illustrates that the values of Q, FOM, and DL are approximately 8×10^4, 1.6×10^4 RIU^{-1}, and 1.2×10^{-8} RIU, respectively. When the frequency point changes in the situation of $\Delta\varphi_2 = 180°$, the values of Q, FOM, and DL are approximately 7.6×10^3, 460 RIU^{-1}, and 3.6×10^{-7} RIU, respectively.

As can be seen in Fig. 6, the displacement of frequency points in the sensing range has a strong linear relationship with the change of RI, and they are fitted as multiple linear functions. By substituting the functions of RI and concentration (Eq.1 and Eq.2) into the fitted function of frequency and refractive index, the relationship between frequency and ambient gas concentration can be obtained. Moreover, because the thickness of the air layer in GSM is larger than that of the hydrogen-sensitive film, the change of the refractive index of the air layer has a
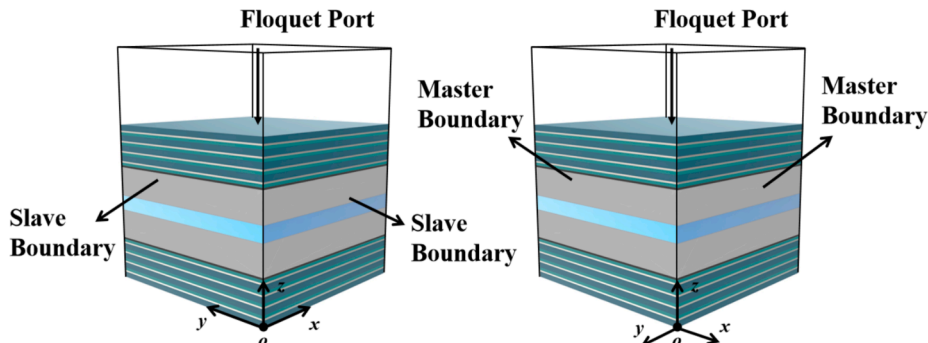
Fig. 4. Simulated port and boundary Settings in HFSS.
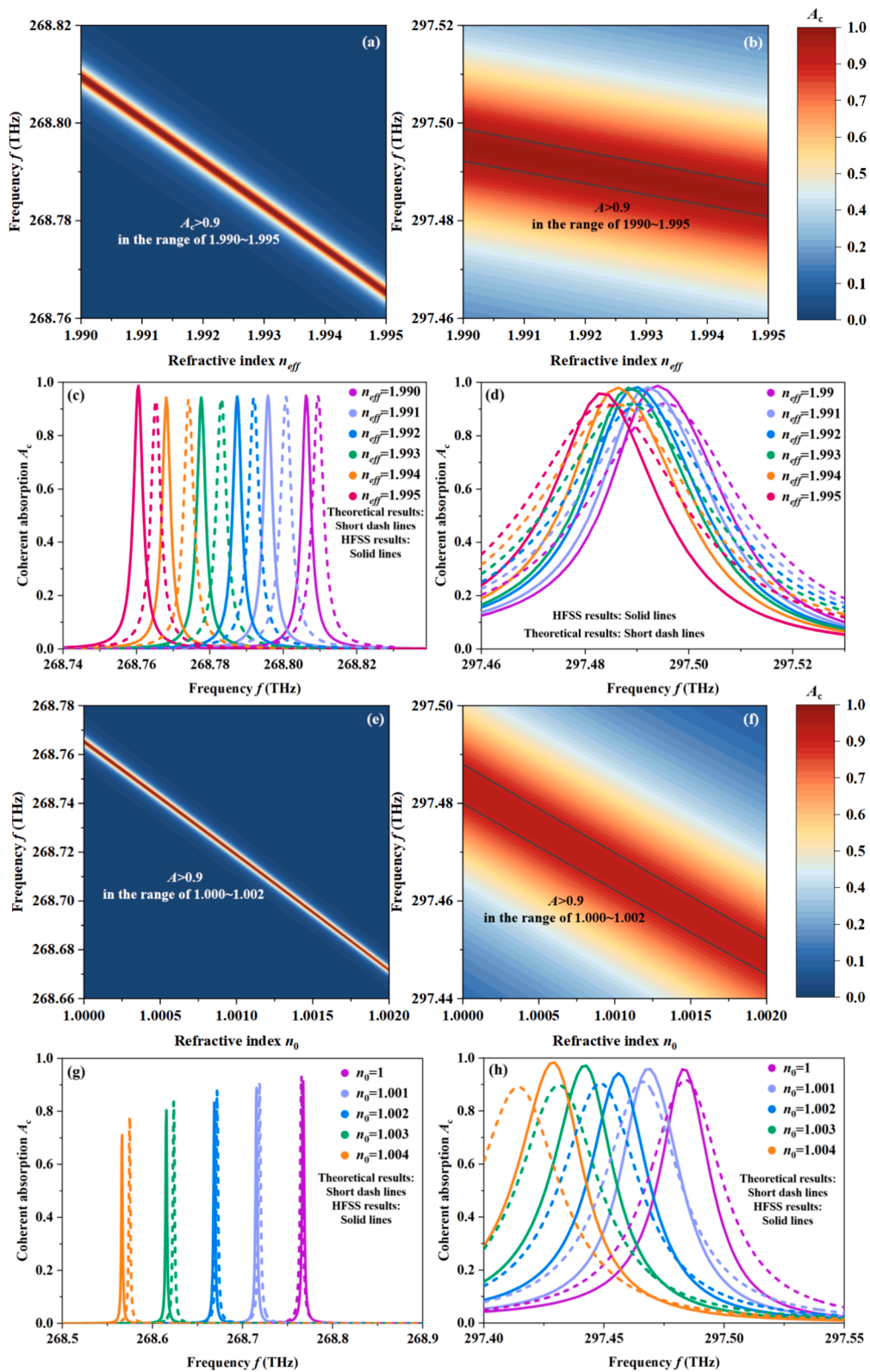
Fig. 5. (a) The frequency point shift in the case of $\Delta\varphi_2 = 0°$ in the range of $1.990 \sim 1.995$ when the GSM senses C_H. (b) The frequency point shift in the case of $\Delta\varphi_2 = 180°$ in the range of $1.990 \sim 1.995$ when the GSM senses C_H. (c) The frequency shift spectral line with the value of n_{eff} in the range of $1.990 \sim 1.995$ in the case of $\Delta\varphi_2 = 0°$. (d) The frequency point shift spectral line with the value of n_{eff} in the range of $1.990 \sim 1.995$ in the case of $\Delta\varphi_2 = 180°$. (e) The frequency point shift in the case of $\Delta\varphi_2 = 0°$ in the range of $1.000 \sim 1.002$ when the GSM senses C_{SO2}. (f) The frequency point shift in the case of $\Delta\varphi_2 = 180°$ in the range of $1.000 \sim 1.002$ when the GSM senses C_{SO2}. (g) The frequency shift spectral line with the value of n_0 in the range of $1.000 \sim 1.004$ in the case of $\Delta\varphi_2 = 0°$. (h) The frequency shift spectral line with the value of n_0 in the range of $1.000 \sim 1.004$ in the case of $\Delta\varphi_2 = 180°$.
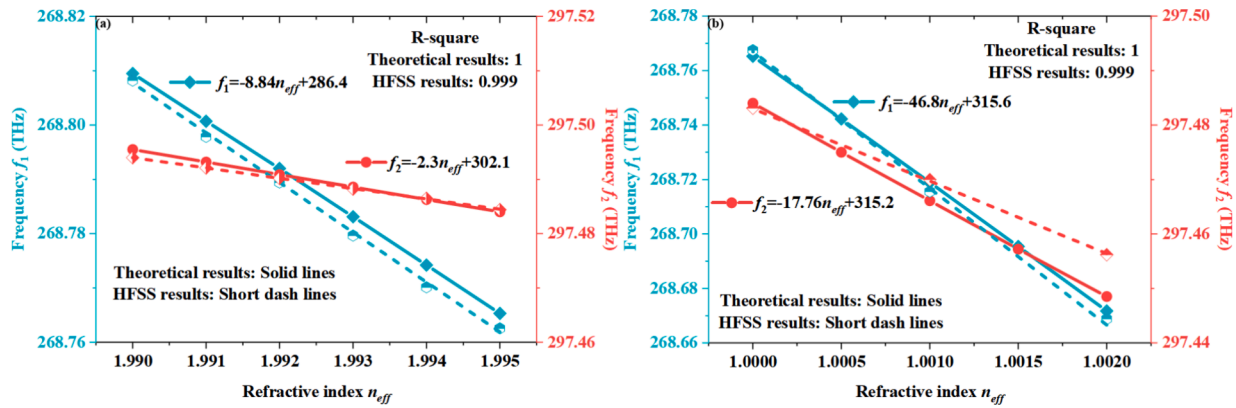
Fig. 6. (a) The linear fitting relationship of C_H sensing in the case of $C_{SO2} = 0$ % within the detection range. (b) The linear fitting relationship of C_{SO2} sensing in the case of $C_H = 0$ % within the detection range.

greater impact on the frequency shift than that of the hydrogen-sensitive film. Because the absorption is highly selective to the frequency, it can accurately detect the characteristic absorption peak of the target gas and improve the sensing sensitivity. Through phase control, multiple absorption peaks of a single gas can be detected simultaneously, thus increasing the applicability and accuracy of the sensing. Since the absorption efficiency of CPA is close to 100 % at a specific frequency, the background interference signal is low, which is conducive to improving the signal-to-noise ratio and detection accuracy. However, nanoscale manufacturing techniques are demanding and may limit large-scale production.

3.4. Performance analysis

The research described above indicates that the suggested GSM, which has a low *DL*, a high *Q*, and an excellent *FOM* when the $\Delta\varphi_2$ is fixed to $0°$, performs well in sensing C_H and C_{SO2}. Moreover, the *S* of the GSM for the same detection range can be changed with CPA, which can realize dual-band sensing and improved sensing accuracy. Its low-sensitivity wavelength can be utilized as a reference to help the high-sensitivity wavelength for sensing, in contrast to typical single-band sensors. Because of its advantage in both H_2 and SO_2 sensing, the GSM may be widely used in industrial H_2 production based on SO_2OR [5]. Because the RI varies are universal, like cells [71]. The work also may be widely used in other fields like aerospace, medicine, and biology.

To verify the experimentability of this work, errors in sample preparation and experimental set-up are introduced and discussed in the supplementary material. The thickness and RI of SiO_2 with errors are respectively considered as d_e and n_e. The work can still achieve the designed sensing performance when d_e is regarded as $(1 \pm 10\%)d_s$, and n_e is defined as $(1 \pm 7\%)n_s$. Even though $\Delta\varphi_2$ in the high sensitivity mode is shifted from $0°$ to $15°$, and $\Delta\varphi_2$ in the low sensitivity mode is shifted from $180°$ to $165°$, the frequency shift is still linear, and there are high absorption peaks. Although this work focuses on theoretical calculation and simulation, the experimental verification of this work is completely feasible through using the existing technology. Some details

about the experimental pieces of equipment are mentioned in section 8 of the supplementary material.

To logically and meticulously demonstrate the advantages of the proposed GSM, a few works about H_2 and SO_2 optical gas sensors done before are included in Table 2, and compared with them. The obtained higher *Q*, lower *DL*, and excellent R-square enable the proposed work to improve gas concentration detection accuracy. In addition, as shown in Table 2, because this work is proposed based on CPA, the GSM has the function of phase control and dual-band sensing.

4. Conclusion

Based on the results of calculation and simulation, it was discovered that the proposed GSM, with the assistance of CPA, can generate APs with different *Q* values, and their frequency points shift due to variations in gas concentration. Through the establishment of a specific linear correlation between the value of RI and frequency point (R-square = 1), the signal of H_2 and SO_2 is translated into the obvious photoelectric signal. As H_2 concentration rises, the frequency points of APs in two modes will increase. In contrast, when SO_2 concentration rises, the two frequency points both decline. Moreover, by modifying the phase of the coherent EWs, the GSM can realize dual-band sensing, which has both high sensitivity and low sensitivity. Thanks to the higher *Q*, and lower *DL* (8.0×10^4 and 1.2×10^{-8} RIU), the sensing of slight difference in gas is possible. The low-sensitivity mode can be utilized as a reference to help the high-sensitivity mode, which can reduce the sensing error compared with typical single-band sensors. This work may be applied in the H_2 production with SO_2 oxidation reaction [5], and it may be significant for future measurement technologies.

CRediT authorship contribution statement

Jia-Hao Zou: Writing – original draft, Investigation, Formal analysis, Data curation. **Jun-Yang Sui:** Visualization, Validation, Resources, Data curation. **Ting-Shuo Yao:** Validation, Software, Resources, Data curation. **Hai-Feng Zhang:** Writing – review & editing, Supervision,

Table 2
The Published Relevant Sensor Compared With The Proposed GSM In Terms of Performance.

Refs.	Q	DL (RIU)	R-square	Sensing gas	Phase control	GSM	Dual-band
[72]	2.0×10^3	1.0×10^{-3}	×	H_2	No	Yes	No
[73]	5.0×10^4	1.0×10^{-5}	×	H_2	No	No	No
[74]	×	×	0.95	H_2	No	No	No
[75]	2.0×10^4	4.7×10^{-1}	0.900	SO_2	No	No	No
[76]	1.6×10^3	3.6×10^{-2}	0.950	SO_2	No	No	No
[77]	1.0×10^4	7.2×10^{-1}	×	SO_2	No	Yes	Yes
This work	8.0×10^4	2×10^{-7}	1.000	H_2 & SO_2	Yes	Yes	Yes

Investigation, Conceptualization.

Funding

This work was supported by the National College Students Innovation and Entrepreneurship Training Program (Grant No.202410293018Z).

Declaration of competing interest

The authors declare that they have no known competing financial interests or personal relationships that could have appeared to influence the work reported in this paper.

Appendix A. Supplementary material

Supplementary data to this article can be found online at https://doi.org/10.1016/j.measurement.2025.116965.

Data availability

Data will be made available on request.

References

[1] N. Sazali, Emerging technologies by hydrogen: a review, Int. J. Hydrogen Energy 45 (2020) 18753–18771.
[2] V. Zgonnik, The occurrence and geoscience of natural hydrogen: a comprehensive review, Earth Sci. Rev. 203 (2020) 103140.
[3] A. Ursua, L.M. Gandia, P. Sanchis, Hydrogen production from water electrolysis: current status and future trends, Proc. IEEE 100 (2012) 410–426.
[4] N.-T. Suen, S.-F. Hung, Q. Quan, N. Zhang, Y.-J. Xu, H.M. Chen, Electrocatalysis for the oxygen evolution reaction: recent development and future perspectives, Chem. Soc. Rev. 46 (2017) 337–365.
[5] A.H.B. Dourado, Opportunities and knowledge gaps of SO2 electrocatalytic oxidation for H2 electrochemical generation, ACS Catal. 9 (2019) 8136–8143.
[6] M. Ball, M. Wietschel, The future of hydrogen – opportunities and challenges, Int. J. Hydrogen Energy 34 (2009) 615–627.
[7] N. Armaroli, V. Balzani, The hydrogen issue, ChemSusChem 4 (2011) 21–36.
[8] J.B. Mudd, Responses of Plants to Air Pollution, Elsevier, 2012.
[9] Z. Lu, Sulfur dioxide emissions in China and sulfur trends in East Asia since 2000, Atmos. Chem. Phys. 10 (2010) 6311–6331.
[10] A.L. Sánchez, E. Fernández-Tarrazo, F.A. Williams, The chemistry involved in the third explosion limit of H2–O2 mixtures, Combust. Flame 161 (2014) 111–117.
[11] N. Dossi, R. Toniolo, A. Pizzariello, E. Carrilho, E. Piccin, S. Battiston, G. Bontempelli, An electrochemical gas sensor based on paper supported room temperature ionic liquids, Lab Chip 12 (2012) 153–158.
[12] J.W. Fergus, Materials for high temperature electrochemical NOx gas sensors, Sens. Actuators B 121 (2007) 652–663.
[13] M.J. Tierney, H.O.L. Kim, Electrochemical gas sensor with extremely fast response times, ACS Publications (2002).
[14] H. Wang, Y. Zhao, H. Ji, Z. Yuan, L. Kong, F. Meng, EEMD and GUCNN-XGBoost joint recognition algorithm for detection of precursor chemicals based on semiconductor gas sensor, IEEE Trans. Instrum. Meas. 71 (2022) 1–12.
[15] J. Pan, Lightweight neural network for gas identification based on semiconductor sensor, IEEE Trans. Instrum. Meas. 71 (2022) 1–8.
[16] J.W. Gardner, P.K. Guha, F. Udrea, J.A. Covington, CMOS interfacing for integrated gas sensors: a review, IEEE Sens. J. 10 (2010) 1833–1848.
[17] Z. Yuan, H. Zhang, J. Li, F. Meng, Z. Yang, H. Zhang, Ag Nanoparticle-modified ZnO–In2O3 nanocomposites for low-temperature rapid detection hydrogen gas sensors, IEEE Trans. Instrum. Meas. 72 (2023) 1–12.
[18] P. Tardy, J.-R. Coulon, C. Lucat, F. Menil, Dynamic thermal conductivity sensor for gas detection, Sens. Actuators B 98 (2004) 63–68.
[19] L. Zhang, J. Hu, Y. Lv, X. Hou, Recent progress in chemiluminescence for gas analysis, Appl. Spectrosc. Rev. 45 (2010) 474–489.
[20] M. Prauzek, An optical-based sensor for automotive exhaust gas temperature measurement, IEEE Trans. Instrum. Meas. 71 (2022) 1–11.
[21] G. Dai, D. Su, X. Qiao, Sensitivity-enhanced high-pressure sensor based on suspended Fiber-Optic Fabry–Pérot interferometer, IEEE Trans. Instrum. Meas. 71 (2022) 1–7.
[22] M.S.P. e Silva, H.P. Alves, H.J.B. De Oliveira, L.H.V. Leão, J.F. Nascimento, J. F. Martins-Filho, Temperature, refractive index, and corrosion simultaneous monitoring using raman anti-stokes reflectometric optical fiber sensor, IEEE Trans. Instrum. Meas. 72 (2023) 1–8.
[23] J. Hodgkinson, R.P. Tatam, Optical gas sensing: a review, Meas, Sci. Technol. 24 (2012) 012004.
[24] J. Hodgkinson, R. Smith, W.O. Ho, J.R. Saffell, R.P. Tatam, Non-dispersive infrared (NDIR) measurement of carbon dioxide at 4.2 μm in a compact and optically efficient sensor, Sens. Actuators B 186 (2013) 580–588.
[25] L.Y. Beliaev, E. Shkondin, A.V. Lavrinenko, O. Takayama, Optical properties of plasmonic titanium nitride thin films from ultraviolet to mid-infrared wavelengths deposited by pulsed-DC sputtering, thermal and plasma-enhanced atomic layer deposition, Opt. Mater. 143 (2023) 114237.
[26] J. Li, H. Yan, H. Dang, F. Meng, Structure design and application of hollow core microstructured optical fiber gas sensor: a review, Opt. Laser Technol. 135 (2021) 106658.
[27] S. Cheng, W. Li, H. Zhang, M.N. Akhtar, Z. Yi, Q. Zeng, C. Ma, T. Sun, P. Wu, S. Ahmad, High sensitivity five band tunable metamaterial absorption device based on block like Dirac semimetals, Opt. Commun. 569 (2024) 130816.
[28] Z. Chen, S. Cheng, H. Zhang, Z. Yi, B. Tang, J. Chen, J. Zhang, C. Tang, Ultra wideband absorption absorber based on Dirac semimetallic and graphene metamaterials, Phys. Lett. A 517 (2024) 129675.
[29] W. Li, S. Cheng, H. Zhang, Z. Yi, B. Tang, C. Ma, P. Wu, Q. Zeng, R. Raza, Multi-functional metasurface: ultra-wideband/multi-band absorption switching by adjusting guided-mode resonance and local surface plasmon resonance effects, Commun. Theor. Phys. 76 (2024) 065701.
[30] W. Li, Y. Yi, H. Yang, S. Cheng, W. Yang, H. Zhang, Z. Yi, Y. Yi, H. Li, Active tunable terahertz bandwidth absorber based on single layer graphene, Commun. Theor. Phys. 75 (2023) 045503.
[31] S. Liang, F. Xu, H. Yang, S. Cheng, W. Yang, Z. Yi, Q. Song, P. Wu, J. Chen, C. Tang, Ultra long infrared metamaterial absorber with high absorption and broad band based on nano cross surrounding, Opt. Laser Technol. 158 (2023) 108789.
[32] B. Shruti, S. Appasani, Pahadsingh, quad-band graphene-based terahertz metamaterial perfect absorber for refractive index sensing, Plasmonics 17 (2022) 2323–2336.
[33] N. Kumar, B. Suthar, C. Nayak, A. Bhargava, Analysis of a gas sensor based on one-dimensional photonic crystal structure with a designed defect cavity, Phys. Scr. 98 (2023) 065506.
[34] K. Zhang, Z. Chen, H. Li, Z. Yi, Y. Liu, X. Wu, A dual-band hydrogen sensor based on Tamm plasmon polaritons, PCCP 25 (2023) 20697–20705.
[35] Shruti, S. Pahadsingh, B. Appasani, A Dual Band THz Metamaterial based Absorber for Gas Refractive Index Sensing, in: 2022 International Conference on Emerging Trends in Engineering and Medical Sciences (ICETEMS), (2022) 173–178.
[36] Y.D. Chong, L. Ge, H. Cao, A.D. Stone, Coherent perfect absorbers: time-reversed lasers, Phys. Rev. Lett. 105 (2010) 053901.
[37] J.-H. Zou, J.-Y. Sui, Q. Chen, H.-F. Zhang, Arithmetic logic unit based on the metastructure with coherent absorptivity, Opt. Lett., OL 48 (2023) 5699–5702.
[38] S. Dey, S. Singh, D.N. Rao, High precision position sensor based on CPA in a composite multi-layered system, Opt. Express, OE 26 (2018) 10079–10090.
[39] D. Yan, R. Mei, M. Li, Z. Ma, Z.H. Hang, J. Luo, Controlling coherent perfect absorptivity via long-range connectivity of defects in three-dimensional zero-index media, Nanophotonics 12 (2023) 4195–4204.
[40] W. Wan, Y. Chong, L. Ge, H. Noh, A.D. Stone, H. Cao, Time-reversed lasing and interferometric control of absorption, Science 331 (2011) 889–892.
[41] D.G. Baranov, A. Krasnok, T. Shegai, A. Alù, Y. Chong, Coherent perfect absorbers: linear control of EWs with EWs, Nat. Rev. Mater. 2 (2017) 1–14.
[42] A. Müllers, Coherent perfect absorptivity of nonlinear matter waves, Sci. Adv. 4 (2018) 6539.
[43] A. Ahmadivand, B. Gerislioglu, Photonic and plasmonic metasensors, Laser Photonics Rev. 16 (2022) 2100328.
[44] S. Cao, X. Fan, W. Fang, M. Du, Q. Sun, H. Niu, C. Li, X. Wei, C. Bai, J. Tao, M. Li, B. Chen, S. Kumar, Multi-function sensing applications based on high Q-factor multi-Fano resonances in an all-dielectric metastructure, Biomed. Opt. Express, BOE 15 (2024) 2406–2418.
[45] Q. Pan, J. Hong, G. Zhang, Y. Shuai, H. Tan, Graphene plasmonics for surface enhancement near-infrared absorptivity, Opt. Express, OE 25 (2017) 16400–16408.
[46] G.W. Hanson, Dyadic Green's functions and guided surface waves for a surface conductivity model of graphene, J. Appl. Phys. 103 (2008) 064302.
[47] L. Qi, Z. Yang, F. Lan, X. Gao, Z. Shi, Properties of obliquely incident electromagnetic wave in one-dimensional magnetized plasma photonic crystals, Phys. Plasmas 17 (2010) 042501.
[48] W. Zhu, F. Xiao, M. Kang, M. Premaratne, Coherent perfect absorptivity in an all-dielectric metasurface, Appl. Phys. Lett. 108 (2016) 121901.
[49] F. Zhang, Mechanically stretchable and tunable metamaterial absorber, Appl. Phys. Lett. 106 (2015) 091907.
[50] S. Das, G.C. Bhar, S. Gangopadhyay, C. Ghosh, Linear and nonlinear optical properties of ZnGeP2 crystal for infrared laser device applications: revisited, Appl. Opt., AO 42 (2003) 4335-4340.
[51] K. Kato, N. Umemura, Sellmeier equations for GaS and GaSe and their applications to the nonlinear optics in GaSxSe1−x, Opt. Lett., OL 36 (2011) 746–747.
[52] H. Liu, M. Wang, Q. Wang, H. Li, Y. Ding, C. Zhu, Simultaneous measurement of hydrogen and methane based on PCF-SPR structure with compound film-coated side-holes, Opt. Fiber Technol. 45 (2018) 1–7.
[53] W. Yang, L.K. Ang, W. Zhang, J. Han, Y. Xu, High sensitivity gas sensor based on surface exciton polariton enhanced photonic spin Hall effect, Opt. Express, OE 31 (2023) 27041–27053.
[54] I.H. Malitson, Interspecimen comparison of the refractive index of fused silica, J. Opt. Soc. Am., JOSA 55 (1965) 1205–1209.
[55] A.K. Geim, Graphene: status and prospects, Science 324 (2009) 1530–1534.

[56] E. Carrasco, M. Tamagnone, J.R. Mosig, T. Low, J. Perruisseau-Carrier, Gate-controlled mid-infrared EWs bending with aperiodic graphene nanoribbons array, Nanotechnology 26 (2015) 134002.

[57] X.-Y. Liang, N. Ding, S.-P. Ng, C.-M.-L. Wu, Adsorption of gas molecules on Ga-doped graphene and effect of applied electric field: a DFT study, Appl. Surf. Sci. 411 (2017) 11–17.

[58] A.S.H. Makhlouf, 1 - Current and advanced coating technologies for industrial applications, Woodhead Publishing (2011) 3–23.

[59] Z. Li, K.A. Khor, Preparation and Properties of Coatings and Thin Films on Metal Implants, in: R. Narayan (Ed.), Encyclopedia of Biomedical Engineering, Elsevier, Oxford, 2019, pp. 203–212.

[60] X. Zhao, Y.C. Shin, Femtosecond laser drilling of high-aspect ratio microchannels in glass, Appl. Phys. A 104 (2011) 713–719.

[61] J.J.J. Kaakkunen, M. Silvennoinen, K. Paivasaari, P. Vahimaa, Water-assisted femtosecond laser pulse ablation of high aspect ratio holes, Phys. Procedia 12 (2011) 89–93.

[62] J.-Y. Sui, J.-H. Zou, S.-Y. Liao, B.-X. Li, H.-F. Zhang, High sensitivity multiscale and multitasking terahertz Janus sensor based on photonic spin Hall effect, Appl. Phys. Lett. 122 (2023) 231105.

[63] L. Grineviciute, Angular filtering by Bragg photonic microstructures fabricated by physical vapour deposition, Appl. Surf. Sci. 481 (2019) 353–359.

[64] S. Wilbrandt, O. Stenzel, N. Kaiser, Experimental determination of the refractive index profile of rugate filters based on in situmeasurements of transmission spectra, J. Phys. D Appl. Phys. 40 (2007) 1435.

[65] K.M. Rabe, C. Ahn, J.-M. Triscone, Physics of ferroelectrics : a modern perspective. Topics in Applied Physics, Springer, 2007.

[66] B.-F. Wan, Q.-Y. Wang, H.-M. Peng, H.-N. Ye, H.-F. Zhang, A Late-model optical biochemical sensor based on OTS for methane gas and glucose solution concentration detection, IEEE Sens. J. 21 (2021) 21465–21472.

[67] E. Özbay, G. Tuttle, M. Sigalas, C.M. Soukoulis, K.M. Ho, Defect structures in a layer-by-layer photonic band-gap crystal, Phys. Rev. B 51 (1995) 13961–13965.

[68] I.L. Lyubchanskii, N.N. Dadoenkova, A.E. Zabolotin, Y.P. Lee, T. Rasing, A one-dimensional photonic crystal with a superconducting defect layer, J. Opt. A Pure Appl. Opt. 11 (2009) 114014.

[69] R. Ozaki, Y. Matsuhisa, M. Ozaki, K. Yoshino, Electrically tunable lasing based on defect mode in one-dimensional photonic crystal with conducting polymer and liquid crystal defect layer, Appl. Phys. Lett. 84 (2004) 1844–1846.

[70] X. Zhang, G. Yu, G. Yuan, Y. Lv, Unidirectional transmission in one dimensional photonic crystal composed of PT symmetric and magneto-optical materials, Opt. Mater. 114 (2021) 110771.

[71] P. Sharma, P. Sharan, P. Deshmukh, A photonic crystal sensor for analysis and detection of cancer cells, In: 2015 International Conference on Pervasive Computing (ICPC), 2015.

[72] L. Kassa-Baghdouche, Gas sensing performance of high-Q photonic crystal nanocavities based on a silicon-on-insulator platform, Opt. Quant. Electron. 53 (2021) 33.

[73] A. Harhouz, A. Hocini, H. Tayoub, Ultracompact gas-sensor based on a 2D photonic crystal waveguide incorporating with tapered microcavity, IOP Conf. Ser.: Mater. Sci. Eng. 1046 (2021) 012001.

[74] Y. Zhang, M. Wang, N. Zhu, B. Han, Y. Liu, Optical fiber hydrogen sensor based on self-assembled PDMS/Pd-WO3 microbottle resonator, Sens. Actuators B 375 (2023) 132866.

[75] J. Nong, Z. Bo, X. Xiao, C. Min, X. Yuan, M. Somekh, F. Fu, Specific designed mid-infrared gas sensor employing bloch surface waves working near the critical angle, SSRN Electron. J. (2022) 1556–5068.

[76] X. Zhao, All-optical photoacoustic detection of SF6 decomposition component SO$_2$ based on fiber-coupled UV-LED, Sens. Actuators B 403 (2024) 135193.

[77] J. Nong, Surface-enhanced mid-IR gas sensor employing wavelength-tunable bloch surface waves, Adv. Theor. Simul. 5 (2022), 2200292.